GEOPHYSICS, VOL. 81, NO. 1 (JANUARY-FEBRUARY 2016); P. E33–E42, 7 FIGS.
10.1190/GEO2014-0583.1

A modeling study of augmenting coarse-grid 3D controlled-source electromagnetics with data from a towed receiver array

Jan Petter Morten[1], Jean-Michael Poudroux[2], and Rune Mittet[1]

ABSTRACT

We have considered the simultaneous 3D inversion of controlled-source electromagnetic data from a towed receiver array and a coarse grid of stationary seabed receivers. Our 3D synthetic model demonstrated the sensitivity and effect on imaging of towed and seabed receiver data. The short-offset data from the towed receivers at 1–3 km offset are effective at resolving a shallow resistor at a 400-m burial depth. On the other hand, the data from the stationary seabed receivers have less noise and will resolve the 3D geometry of resistive structures buried at the 1–2 km depths typical of a hydrocarbon reservoir. We have determined how the complementary sensitivity of data from the two receiver types can be used in simultaneous inversion to recover the shallow and deep resistors.

INTRODUCTION

The marine controlled-source electromagnetic (CSEM) method is used to determine resistivity below the seafloor. An review of the basic concepts of the method is given by Constable and Srnka (2007). Towed receiver systems have been suggested as a useful complement to the CSEM survey technique using seabed receivers, with applications for, e.g., mapping of shallow gas hydrates (Weitemeyer and Constable, 2010; Goswami et al., 2013) through acquisition of 2D inline profiles (Mattsson et al., 2012). In a survey involving towed receivers, the CSEM source and electric field sensors are towed behind the vessel. The towed receivers then record data at ranges given by the tow cable length. The source-receiver offset may vary due to, e.g., feathering, but the towed receiver data are nominally acquired at fixed offsets. The largest offset range acquired using a towed receiver array can be limited by the operational complexity of towing a long cable close to the seafloor. The receivers along the cable must be navigated accurately to ensure high data quality, and avoid impact with the seafloor. An unstable or fluctuating flight path through the seawater can also lead to large noise on the towed receiver measurements. However, high-frequency, short-offset data from a towed receiver array can be useful for mapping resistors down to a few hundred meters below the seafloor.

Compared to the data from stationary seabed receivers typically used in 3D state-of-the-art CSEM surveys, the data from towed receivers will suffer from larger noise levels due to motion. However, as described by Constable et al. (2012) this is mainly a problem for low frequencies. Hydrocarbon exploration is typically carried out in sedimentary basins. In such areas, the typical rock resistivity dictates that it is the higher frequencies in the range 1–10 Hz that are of the greatest interest for the towed receivers because one is typically constrained to shorter offsets.

In a 3D CSEM survey, receivers are distributed over an area. A target region may then be sampled at variable azimuthal angle and over the measurable range of the CSEM source signal. This enables imaging of targets at depth and laterally. Because the horizontal electric dipole source used is a vector source, different polarizations are measured by receivers that are inline, broadside, or at an intermediate azimuthal angle relative to the source. The variable polarization measurements in 3D acquisition enhances sensitivity to various subsurface structures. Acquisition of coarse-grid 3D CSEM data is an effective tool for reducing exploration drilling risk in frontier areas. In field data examples described by Gabrielsen et al. (2013), the receiver grid node separation is 3 km. The data analysis with correlation to known discoveries shows that 3D CSEM can be used as a decision-making tool for initial interpretation, risking, and reserves estimation in frontier areas. The 3×3 km receiver grid provides a cost-effective scan of a large area. The sensitivity toward targets located between source towlines is sustained in a 3D acquisition by the azimuthal data recorded by receiver lines offset from the source towlines (Morten et al., 2009).

Manuscript received by the Editor 10 December 2014; revised manuscript received 18 June 2015; published online 22 December 2015.
[1]Electromagnetic GeoServices (EMGS), Trondheim, Norway. E-mail: jpmorten@emgs.com.
[2]Norwegian University of Science and Technology, Department of Physics, Trondheim, Norway. E-mail: jpoudroux@emgs.com.

In order for imaging and inversion to get a good result, it is important that the whole offset range in which data are sensitive to a resistive feature is recorded. The onset of the largest sensitivity toward a resistor in the CSEM data will typically take place at shorter offsets for more shallow burial depths. Imaging of the lateral geometry of the resistor imposes the additional requirement that the relevant offset range is sampled evenly over the survey area. The offset-dependent sensitivity is taken into account in survey planning and optimization. In this paper, the target level is about 1–3 km burial depth. This target level is reflected in the choice of seafloor node separation. We will refer to a resistor at significantly shallower burial depth as a shallow resistor. Such resistors could be due to lithology or gas hydrate accumulations that can occur at a few hundred meters below the seafloor for the water depths we consider (Xu and Ruppel, 1999).

The increased receiver and towline separation in coarse-grid data acquisition implies that the lateral sampling density is reduced. One way to visualize the depth-dependent impact of the reduced sampling density is to plot the common midpoint (CMP) positions of the survey data at varying source-receiver offset, shown in Figure 1. The lateral location of a CMP position is correlated to the region of largest sensitivity, which can be computed by modeling. This concept has been used in Mittet et al. (2007) for inversion of line data based on 1D modeling of CMP gathers.

At offsets in the same range as the receiver position spacing or shorter, the CMPs will be unevenly distributed over the survey area. The CMPs in this range will be located at positions in between receiver positions and along the source towlines. An example of this effect is shown in Figure 1a, where we have plotted the CMP positions of the data at a 2-km offset for a grid of seafloor nodes with spacing of 3 km. We will refer to the offset range below the receiver separation as short offsets, and we expect that the uneven distribution of offsets in this range will impact the imaging of shallow resistors. At longer offsets corresponding to the onset of sensitivity from more deeply buried targets, the CMPs will be more evenly distributed over the survey area and cover the area close to receiver positions as well as regions between source towlines. This is shown in Figure 1c.

An interesting option to increase the short-offset sampling density to improve imaging of shallow resistors in coarse-grid 3D CSEM data is to deploy an array of towed receivers for recording at the same time as the source is towed for the stationary seabed

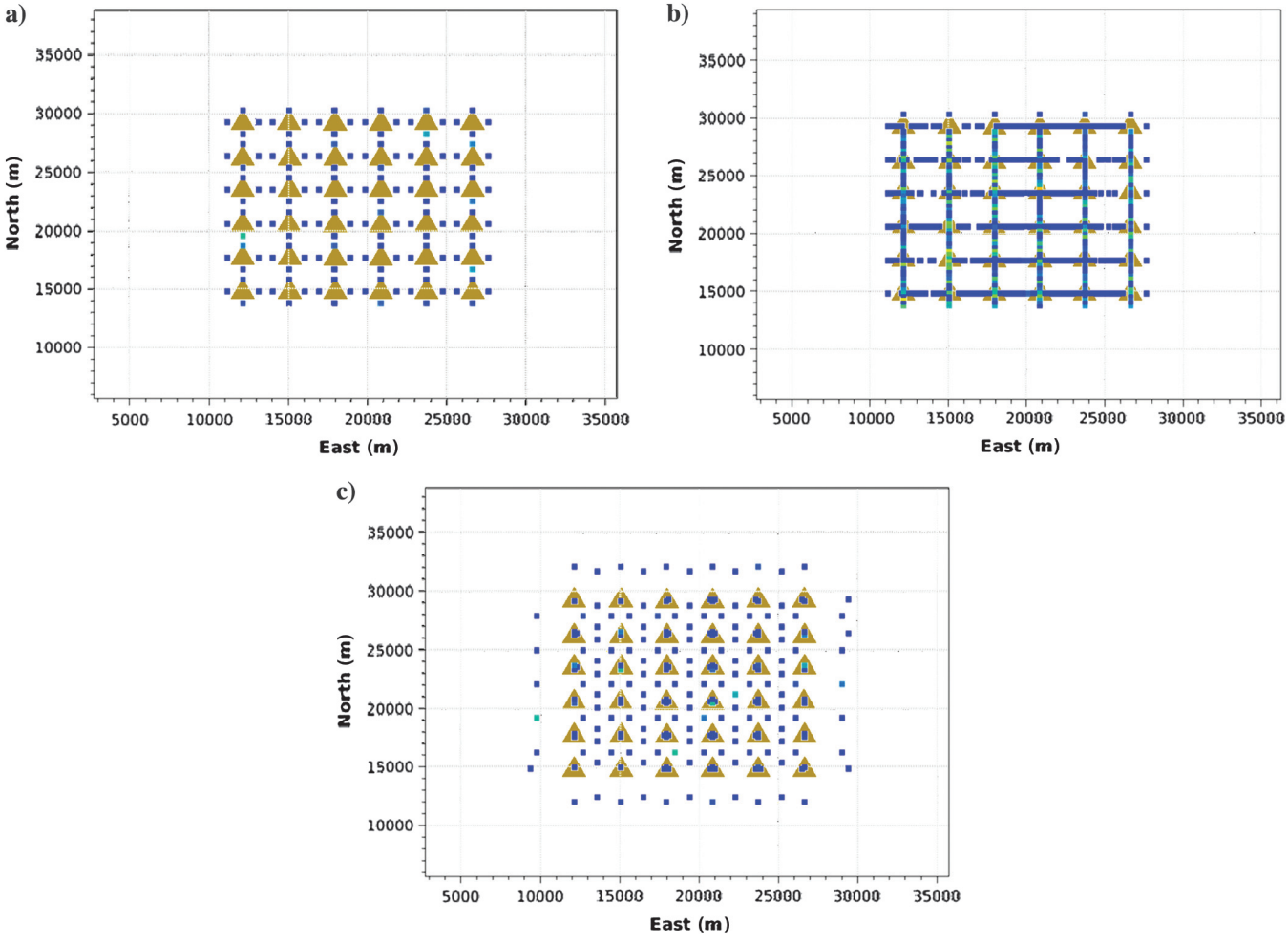

Figure 1. CMP positions for data points at fixed offsets. The yellow triangles show receiver positions, and the blue and green squares show the CMP position of the data. The receiver spacing in these examples is 3 km. More details of the survey layout can be seen in Figure 2. (a and b) 2-km offset and (c) 5.5-km offset. In panel (a), we included only the data from seabed receivers.

receivers. An illustration of the increased sampling is shown in Figure 1b, in which the CMP positions for data from towed receivers have been included. We will consider towing where the source and the receiver array are at a depth close to the seafloor. Towing of a receiver array of 1070 m total length at less than 100 m elevation over the seafloor is already demonstrated by Constable et al. (2012). Because the same source is used for measurements at the towed and stationary receivers, the data can be acquired with little increase in vessel time. However, the increased operational complexity can make the survey more demanding to acquire. Real-time monitoring of navigation and stability of the deep-towed array must be ensured to avoid impact with the seafloor in case of abrupt bathymetry variations. Towing line turns can also be more time demanding.

In this paper, we consider 3D inversion of synthetic CSEM data from a towed receiver array as well as stationary seabed receivers. We inverted data from a model with targets representing typical hydrocarbon reservoirs at various burial depths as well as a large-scale, very shallow thin resistor. The burial depths considered for the hydrocarbon targets are 1, 1.5, and 2 km, which correspond to some typically encountered exploration scenarios. The inversions are carried out using either data from the towed or stationary receivers alone or we include data from both receiver types in combination. We will study the effect on imaging for the three data combinations. Finally, we discuss the detection sensitivity and imaging criteria and how our results illustrate the expected relationship between imaging quality and offset-dependent sampling.

SURVEY LAYOUT AND INVESTIGATED MODEL

We will consider the inversion of synthetic data from the survey layout illustrated in Figure 2. The data set has in total 12 source towlines in two orthogonal directions, x and y. The source is towed at a constant elevation 30 m above the seabed, and the water depth is 1 km. The 36 stationary seabed receivers record the horizontal components of the electric and magnetic fields for all the source towlines. The spacing between the seabed receiver stations is $L = 2.9$ km, and the source positions for these receivers were simulated at 100-m intervals along the towlines. We expect that our results would be invariant from increasing this interval to the length of the source dipole, which is 270 m. All data points at offsets from 1 up to 10 km were considered unless the magnitude fell below the noise levels specified below in the section "Uncertainty model."

Along the source towlines, we have also simulated data for a towed array of three receivers. The towed receivers are located at fixed offsets of 1.0, 2.0, and 3.0 km behind the source at the same elevation as the source. A towed receiver will typically be able to record high-fidelity data only along an axis parallel to the towing direction. Thus, a towed receiver equipped with electric and magnetic recording equipment can measure the E_x- and H_x-components for an x-directed towline. However, due to the inline nature of the towed receiver configuration, there will only be significant measured amplitudes on the electric channel. The towed receivers described in Constable et al. (2012) also record E_z-component measurements. In this paper, we have included electric field data points at every $dL = 300$ m interval along the towlines for each of the towed receivers. The inversion software we will use is gradient-based, and the numerical cost then scales with the number of receiver positions. The choice of a larger interval dL for towed receivers then reduces the computational load in the inversion. Note, however, that due to the propagation length scales involved, the results are not expected to change significantly if dL were reduced.

The parameters of the deep-towed receiver array configuration studied in this paper do not correspond to an equipment set from which data have been published. However, a similar setup has been developed and deployed by Scripps Institution of Oceanography. For the deployments so far, the farthest offset reported is about 1 km and the deepest towing depth has been 4 km (S. Constable, personal communication, 2015). In this study, we include data from a receiver at a 3-km offset. Although the towed receiver array cable in this case is considerably longer, we do not consider such an acquisition to be prohibitively more complex. However, it is likely that the operational window for this system will be more restricted. For example, it could require that the bathymetry varies gently along the survey towing lines and that seafloor ocean currents are weak. The towed receiver array and cable would be designed with neutral buoyancy. The towing elevation of 30 m considered here could be extended to, e.g., 100 m to increase the safety of the operations. Such an elevation increase will have an insignificant effect on data quality for the frequencies considered. This is because the relevant skin depth governing signal attenuation in water is significantly larger than this increase of towing elevation. The towed receivers could be fitted with real-time elevation monitoring, so that impact with the seafloor can be avoided by making adjustments to the towing during the acquisition.

The source frequencies are the same for the towed receivers and stationary seabed receivers. The simulated acquisition implies that

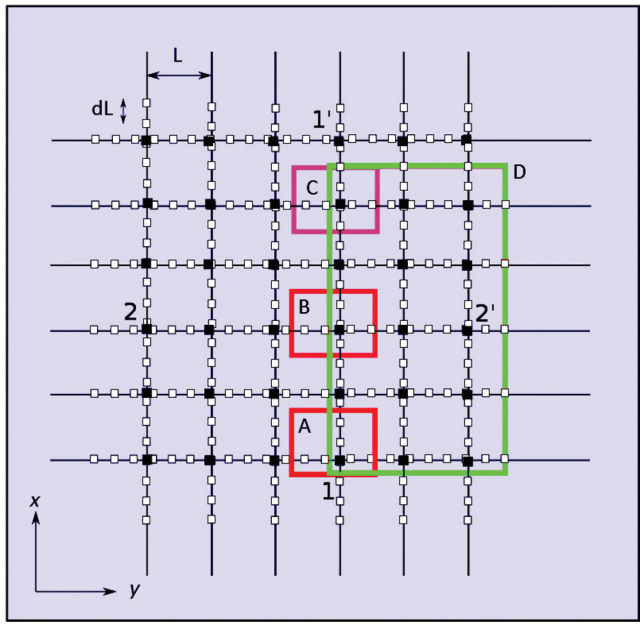

Figure 2. Schematic survey layout and lateral resistor outlines (red and green). The black and white dots illustrate the stationary seabed and the towed receiver locations, respectively. The burial depths are 1000, 1500, 2000, and 400 m for resistors A, B, C, and D, respectively. Resistors A, B, and C (red outlines) have resistivity of 100 Ωm and they measure $3000 \times 5000 \times 100$ m^3. Resistor D (green outline) has resistivity of 10 Ωm and it measures $15000 \times 8000 \times 50$ m^3. The towline and stationary receiver spacing is $L = 2900$ m, and the towed receivers have a data point separation of $dL = 300$ m.

the same source is used for both receiver types. We included frequencies of 0.8, 1.3, 2.0, and 3.2 Hz in our data set. For short offsets, low-frequency data responses will typically be dominated by direct propagation through seawater or propagation along the seabed (Løseth, 2011), whereas higher frequencies can give valuable information about the shallower parts of the formation even at a short offset. In our survey, we have therefore chosen to include higher frequencies than might typically be considered in hydrocarbon exploration in a high-conductive/low-resistive background. This will ensure that the towed receiver data have good sensitivity to the shallow structure. The low frequencies give sensitivity to the deeply buried hydrocarbon reservoir targets.

We consider a model with a constant water depth of $z_{\mathrm{wd}} = 1$ km and homogeneous water resistivity of 0.25 Ωm. Seawater resistivity varies with temperature, among other parameters, and in survey data acquired in a mild climate, the water resistivity can be lower than this value, and it can vary considerably with depth. In such cases, a vertical resistivity profile in the water column must be incorporated. The total lateral size (x- and y-dimensions) of our model is 44×44 km, and the total depth (z) is 5.0 km. The background resistivity varies with all three coordinates, and it is given by the following bilinear form:

$$\rho(x, y, z) = \rho_0 + a(z - z_{\mathrm{wd}}) + b(z - z_{\mathrm{wd}})(x + y), \qquad (1)$$

such that the resistivity just below the seabed is $\rho_0 = 1.0$ Ωm and the maximum resistivity at approximately 10 Ωm is reached at the largest depth in the top right (maximal x and y) corner of the model. The resistivity increase with x, y, z is controlled by the parameters $a = 10^{-3}$ Ω and $b = 1.175 \cdot 10^{-5}$ Ω/m. In the present study, we consider an isotropic model. With respect to the main conclusions of this study, we consider that an anisotropic model study would give similar conclusions.

Four resistors are embedded in our model. The lateral extents of these resistors are indicated in Figure 2. In the figure, the resistors are labeled A, B, C, and D. The three targets A-C represent typical hydrocarbon reservoirs at various burial depths of 1.0, 1.5, and 2.0 km below the seabed. The thicknesses and resistivities of these targets are identical and are equal to 100 m and 100 Ωm. Resistor D represents a regional shallow resistor and is buried 400 m below the seabed. Resistor D has a lower thickness and resistivity than the targets. The thickness of resistor D is 50 m, and its resistivity is 10 Ωm. The lateral extent of targets A-C is 3×5 km. Resistor D is much larger at 15×8 km, and it has a partial lateral overlap with all the targets.

UNCERTAINTY MODEL

The synthetic data were contaminated by noise at realistic levels. The inversion results thus reflect the resolution and imaging quality that could be achieved from real data. We added two types of noise, which we will refer to as ambient noise and relative uncertainty (Mittet and Morten, 2012). The contamination of data with noise is described by the following transformation:

$$E_i(\mathbf{r}|\mathbf{r}', \omega) \rightarrow (1 + \alpha)E_i(\mathbf{r}|\mathbf{r}', \omega) + \eta(\omega). \qquad (2)$$

In this expression, $E_i(\mathbf{r}|\mathbf{r}', \omega)$ is the electric field component i at position $\mathbf{r}$ due to a dipole source at position $\mathbf{r}'$ operating at angular frequency ω. The relative uncertainty and ambient noise contributions are modeled by α and η, respectively. These quantities are complex random variables with Gaussian distributed real and imaginary parts of mean zero and standard deviations $\delta\alpha/\sqrt{2}$ and $\delta\eta/\sqrt{2}$, and we define the standard deviation of the data in terms of the noise-free quantity as $\delta E_i = \sqrt{(|E_i|\delta\alpha)^2 + (\delta\eta)^2}$. The factor α is dimensionless, and η has the unit V/m for the measured field and $\mathrm{V/Am^2}$ for data normalized to the source dipole moment. The ambient noise standard deviation typically varies with frequency, but in this paper, we will consider a simplified situation in which the standard deviation is a constant.

The ambient noise level describes effects due to, e.g., magnetotelluric signals, noise from receiver motion and ocean swell, and receiver electronics. The receiver electronics noise typically increases with decreasing frequency, i.e., $1/f$-noise. The magnetotelluric noise depends on e.g., solar activity and time of day, and the ocean swell noise depends on weather conditions. The ambient noise would be present in the data even though the source was not transmitting. Motion noise effects arise whenever the sensor equipment is moving in the environment of the conductive seawater and the earth magnetic field. We expect that such contributions will be significantly higher for towed receivers moving through the seawater than stationary seabed receivers, which can be designed to minimize movement from seabed positions; see, e.g., the experimental data in Constable et al. (2012) and Weitemeyer and Constable (2012). However, the measured frequency dependence of such noise contributions on towed receivers indicates that noise floors of magnitude 3×10^{-10} V/m can be achieved in the frequency range of 1–10 Hz. The corresponding number for a seafloor node receiver can be an order of magnitude lower. In this paper, we will consider that the data have been normalized by the source dipole moment. Assuming a source dipole moment representative of commercial equipment 3×10^5 Am, the normalized data noise floor becomes $\delta\eta_{\mathrm{seabed}} = 10^{-16}$ $\mathrm{V/Am^2}$ for stationary seabed receivers and $\delta\eta_{\mathrm{towed}} = 10^{-15}$ $\mathrm{V/Am^2}$ for towed receivers. In the synthetic data, the source dipole is simulated as an extended dipole 270 m long by integrating a line of point dipoles. We then consider normalized data corresponding to a unit dipole moment.

The relative uncertainty factor describes the effect from fluctuations in, e.g., the source position or source current amplitude, as well as the corresponding uncertainty in the receiver positioning and sensor calibration. The magnitude of this noise contribution is proportional to the magnitude of the electric field at the receiver position due to the CSEM electric dipole source. Contributions to the relative uncertainty factor from any fluctuations in source parameters will similarly affect the stationary seabed and towed receivers. However, the data from towed receivers will suffer from larger effects of navigation uncertainty due to the less accurate dynamical positioning. The position and orientation of the stationary receivers can be determined very accurately by stacking many independent measurements of their position. To obtain a quantitative measure for $\delta\alpha$, we use the error propagation techniques described by Mittet and Morten (2012). Error propagation analysis can determine the aggregate uncertainty from the sum of equipment-characteristic properties such as the fluctuation in, e.g., the offset, orientation, and calibration of a single receiver.

Mittet and Morten (2012) describe an equipment setup for stationary seabed receivers that results in $\delta\alpha_{\mathrm{seabed}} = 0.03$. This setup is characterized by relative uncertainty in the source current, source dipole length, and receiver calibration — all at 1%. Further, for the

source, the uncertainty in the pitch orientation angle is $\pm 1°$. The positioning uncertainty for the source-receiver system in the towing direction is ± 15 m, and in the vertical direction it is ± 5 m. A detailed error propagation analysis for this parameter setup is given in Mittet and Morten (2012), and we will assume the same parameters for the stationary receiver data in this paper.

Figure 3 shows the effect of the noise contamination according to equation 2 for the stationary seabed receiver over target A. We show the actual contaminated data amplitude and phase that will be the input to inversion, but also the normalization of contaminated data $E_x^{\text{contaminated}}$ to the modeled synthetic responses without added noise E_x^{clean}. The effect of the ambient noise is very clear in the far-offset data in Figure 3a, where the amplitude and phase become random when the signal amplitude approaches the lowest value 10^{-16} V/Am^2. The effect of relative uncertainty noise is not clear in a logarithmic scale plot, but the normalization $E_x^{\text{contaminated}}/E_x^{\text{clean}}$ shown in Figure 3b demonstrates how the contaminated data have random fluctuations at large signal amplitudes also. The typical fluctuation ± 0.03 from the nominal level 1.0 in the top panel of Figure 3b corresponds to the standard deviation $\delta\alpha$. For the phase in the lower panel, the typical fluctuation $\pm 2^{\circ}$ corresponds to $180\delta\alpha/\pi$.

The asymmetry of in-towing and out-towing that can be seen in the phase between offsets 2.5–5 km for the receiver data shown in Figure 3a is an indication of the presence of target A. To give a clearer impression of the inline data sensitivity to targets A, B, and C in seabed receiver data, we show in Figure 4 the difference between the synthetic data for the background model (see equation 1) and the noise-contaminated modeled forward responses. The anomalies due to targets A and B are very clearly visible, and the magnitude of the response is on order of 25 standard deviations of the contaminated data. The response from target C is not equally easy to discern in this plot because it is mixed with the response from shallow resistor D of similar magnitude — about 15 standard deviations.

We now consider the relative uncertainty for towed receiver data $\delta\alpha_{\text{towed}}$. We assume the same uncertainty parameters for the source, but contributions from fluctuations in the positioning and orientation of the towed receivers can give a larger total uncertainty. The absolute positioning of the towed receivers can be less accurate than for the stationary seabed receivers. For the short-offset data considered here, Mittet and Morten (2012) show that the uncertainty is particularly sensitive to errors in the inline source-receiver offset, which is typically a small contribution at larger offsets. The contribution to the total uncertainty from these errors is proportional to the magnitude of the spatial derivative in the inline direction of the field, rather than the field magnitude itself. Due to the rapid decay of the field magnitude at a short offset, this contribution can exceed other contributions. The effect is also larger at a higher frequency. We have carried out modeling studies using parameters corresponding to the measurement configuration and model described in this paper, and we studied the ratio of the uncertainty from inline position errors to a 3% relative uncertainty $\partial_x|E_x|\delta x/(|E_x|\delta\alpha)$. In this expression, the inline positioning fluctuation $\delta x = 15$ m is set equal to the value used for seabed receivers in the example from Mittet and Morten (2012) referred to above. The ratio is close to 1.8 for the frequencies most relevant for the towed receiver data, and it varies on the scale of ± 0.3 for the offsets 1–3 km considered. We therefore approximate the effective towed receiver relative uncertainty $\delta\alpha_{\text{towed}} = 0.06$ from adding the variances.

To illustrate the effect of the noise on the towed receiver data, we show in Figure 5 the inversion input data responses from the towlines aligned with the profiles 1-1′ and 2-2′ from Figure 2. The towed receiver data at 3.2 Hz for the different offsets are color coded, and the responses are plotted at the source-receiver CMP position. For the offsets considered in this paper, the data ampli-

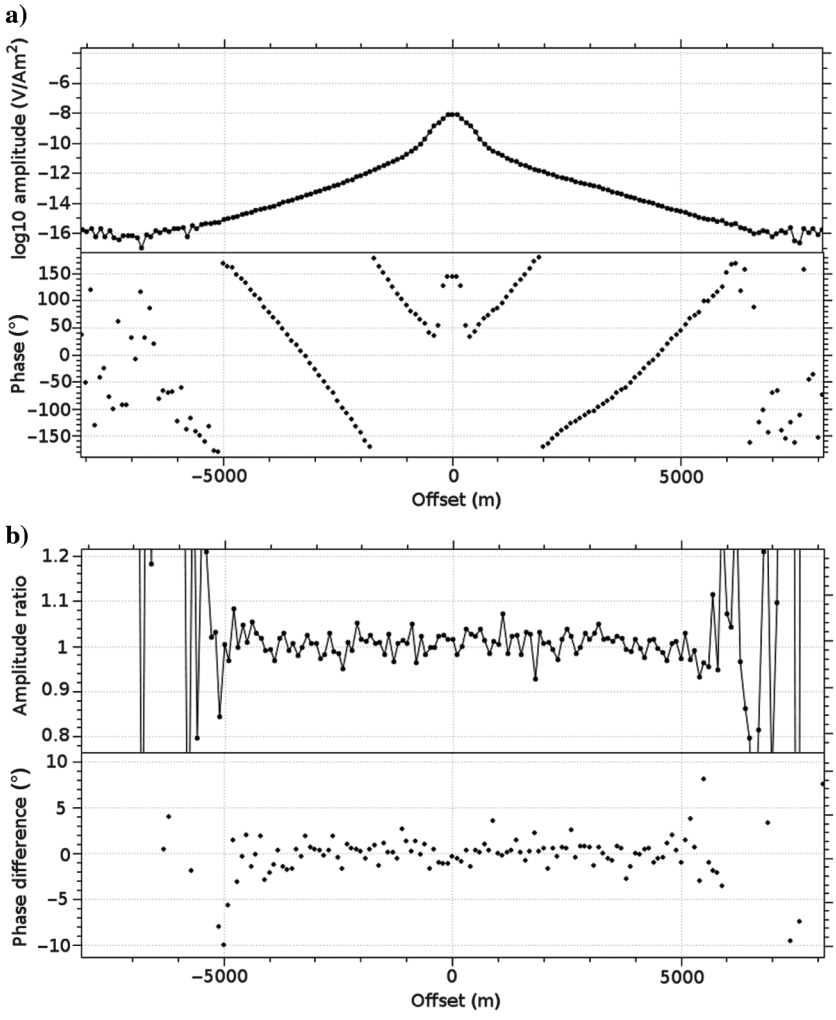

Figure 3. E_x data at 2.0 Hz for the seabed receiver located over target A for the inline towing along the profile 1-1′ in Figure 2. Panel (a) shows the amplitude [V/Am^2] (top) and phase (deg) (bottom) for the data after contamination with noise. Panel (b) shows the contaminated data normalized to the clean synthetic data, i.e., the amplitude (top) and phase (bottom) of $E_x^{\text{contaminated}}/E_x^{\text{clean}}$.

tudes are significantly larger than the ambient noise level $\delta\eta_{\text{towed}}$ for all frequencies included. Even at the farthest offset (3 km) and highest frequency (3.2 Hz), the signal-to-noise ratio is close to 10. Thus, the errors in the data are dominated by the relative uncertainty.

The offset variation seen in Figure 5 can be correlated to target positions, and it demonstrates the sensitivity of the towed receiver data. From Figure 5a and 5c, we can see that target A has a clear impact on the data especially for the towed receivers at the 2- and 3-km offsets. The shortest source-receiver offset of 1 km has a low target sensitivity due to the dominating contribution from the propagation only through seawater or along the seafloor. Further, the data responses from the deeper targets B and C constitute small effects on the scale of the measurement error or less at all the towed receiver offsets. The shallow resistor D is seen from Figure 5b and 5d to have a clear impact on the data. The lower frequencies in the data set have similar qualitative features as the data shown in the figure, but the relative resistor responses are weaker (not shown).

INVERSION

We carried out isotropic 3D inversion for three cases of data selection: (1) only data from seabed receivers, (2) only data from towed receivers, and (3) a combined data set with the seabed and towed receivers. We use the limited-memory Broyden-Fletcher-Goldfarb-Shanno optimizer described in Zhu et al. (1997) and a finite-difference time-domain forward solver described in Maaø (2007). To reduce computational cost, we used the reciprocity principle for the towed receiver data (also for seabed receivers). This means that our data are organized such that the towed receiver array is represented as a single receiver but with three associated source positions at each demodulated source position.

The number of data points from the seabed receivers N_{seabed} will be much larger than the number of data points from the towed receivers N_{towed} because the seabed receivers will record signals not only from the source towline crossing over the receiver position, but also from all the other towlines at which the source generates a signal above the noise level. For the survey shown in Figure 2, we had $N_{\text{seabed}}/N_{\text{towed}} \approx 33$ and $N_{\text{seabed}} \approx 0.5 \times 10^6$. To balance the influence of the two data types in the inversion cost function, we normalize each data type contribution by the number of samples:

$$\varepsilon_{\text{data}}(\sigma) = \frac{1}{N_{\text{seabed}}}\varepsilon_{\text{seabed}}(\sigma) + \frac{1}{N_{\text{towed}}}\varepsilon_{\text{towed}}(\sigma), \qquad (3)$$

where the cost function terms in this expression are computed using the $L2$ norm, e.g.,

$$\varepsilon_{\text{seabed}}(\sigma) = \sum_{i,\kappa}\left|\frac{E_i^{\text{synthetic}}(\kappa,\sigma) - E_i^{\text{observed}}(\kappa)}{\delta E_i^{\text{observed}}(\kappa)}\right|^2, \qquad (4)$$

where σ is the conductivity model. Index κ labels all contributing data points, i.e., the index spans the range of frequencies ω and source-receiver coordinates $\{(\mathbf{r}_{\text{Rx}}, \mathbf{r}_{\text{Tx}})\}$ of the measurements in the input data set. We defined $\delta E_i^{\text{observed}}(\kappa)$, which is the estimated uncertainty of the samples, calculated using the standard deviations of α and η of the noise model in equation 2. We also include a total variation regularization term $\varepsilon_{\text{regularization}}(\sigma)$ in the cost function, which acts to smooth the reconstruction laterally. The cost function to be minimized is thus $\varepsilon(\sigma) = \varepsilon_{\text{data}}(\sigma) + \varepsilon_{\text{regularization}}(\sigma)$, with the conductivities of a rectilinear grid representation $\sigma(\mathbf{r}) \rightarrow \sigma(\mathbf{r}_{lmn})$ as the parameters for the l, m, n spatial indices of the discretization.

The quasi-Newton optimizer requires that we compute the gradient of the misfit function with respect to the optimization parameters. The gradient following from equation 4 can be computed in the discretized representation as

$$\begin{aligned}\frac{\partial\varepsilon_{\text{seabed}}(\sigma)}{\partial\sigma(\mathbf{r}_{lmn})} &= \sum_{i,\omega,\mathbf{r}_{\text{Rx}},k=x,y,z} G_{ki}^{EJ}(\mathbf{r}_{lmn}|\mathbf{r}_{\text{Rx}},\omega,\sigma) \sum_{j,(\mathbf{r}_{\text{Rx}},\mathbf{r}_{\text{Tx}})} G_{kj}^{EJ}(\mathbf{r}_{lmn}|\mathbf{r}_{\text{Tx}},\omega,\sigma) \\ &\times \frac{[E_i^{\text{synthetic}}(\mathbf{r}_{\text{Rx}}|\mathbf{r}_{\text{Tx}},\omega,\sigma) - E_i^{\text{observed}}(\mathbf{r}_{\text{Rx}}|\mathbf{r}_{\text{Tx}},\omega)]^*}{[\delta E_i^{\text{observed}}(\mathbf{r}_{\text{Rx}}|\mathbf{r}_{\text{Tx}},\omega)]^2} V_{lmn} d_j(\mathbf{r}_{\text{Tx}}) + \text{c.c.}\end{aligned} \qquad (5)$$

In this expression, the Green's function $G_{ki}^{EJ}(\mathbf{r}_{lmn}|\mathbf{r},\omega,\sigma)$ determines the electric field in direction k at a grid position given by indices l, m, n due to a unit electric source in direction i at position $\mathbf{r}$; V_{lmn} is the volume of the grid cell at index l, m, n; $d_j(\mathbf{r}_{\text{Tx}})$ is the orientation vector of the source at position $\mathbf{r}_{\text{Tx}}$; and c.c. indicates the complex conjugate of the preceding term. This expression for the gradient demonstrates how the numerical cost of the quasi-Newton

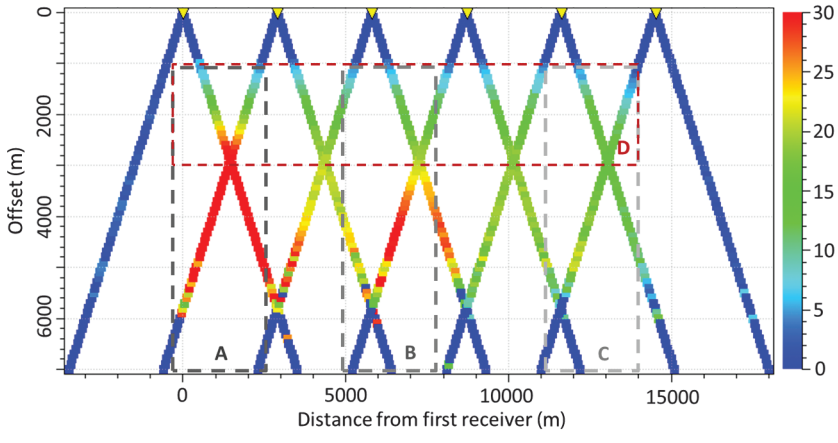

Figure 4. Target responses at 2.0 Hz for the six seabed receivers and the towline along profile 1-1′ in Figure 2 in units of standard deviations $|E_x^{\text{background}} - E_x^{\text{contaminated}}|/\delta E_x^{\text{contaminated}}$. This figure shows the in-tow and out-tow for each receiver. Dashed lines show the approximate location of the main response from resistors A-C (gray) and D (red).

optimizer scales with the number of receivers, but not the number of sources, by using superposition in the computation of the last sum.

DISCUSSION AND INVERSION RESULTS

All inversions shown converged on a model in which the misfit was on the scale of the noise added to the data (i.e., rms error ≈ 1). The initial model corresponded to the true model background. Figure 5 illustrates this for the towed receiver data in the case in which we inverted the towed receiver data and the seabed receiver data. Figure 6 shows depth slices at the depth of the shallow resistor D. Figure 7 shows cross sections along two orthogonal towlines.

We first discuss the imaging results for shallow resistor D. The result in Figure 6a shows that the coarse-grid seabed receiver data could not properly reconstruct the geometry of the thin, shallow resistive layer. The layer is recovered only at locations close to the receivers, and a conductive artifact is introduced directly underneath receiver locations. We understand this to be a consequence of the very limited short-offset data coverage. Although the farther offsets are sensitive to the presence of resistor D and the inversion is able to fit these data, there is insufficient information to geometrically reconstruct the resistor properly. The results shown in Figure 7a and 7b further illustrate that the vertical resolution of the resistor D is poor.

The inversion result in which only the data from towed receivers were used, Figure 6b, shows a more consistent reconstruction of resistor D along the towlines. The short-offset data from the towed receiver array thus had sensitivity and sufficient sampling at variable offset so that the geometry could be reconstructed. However,

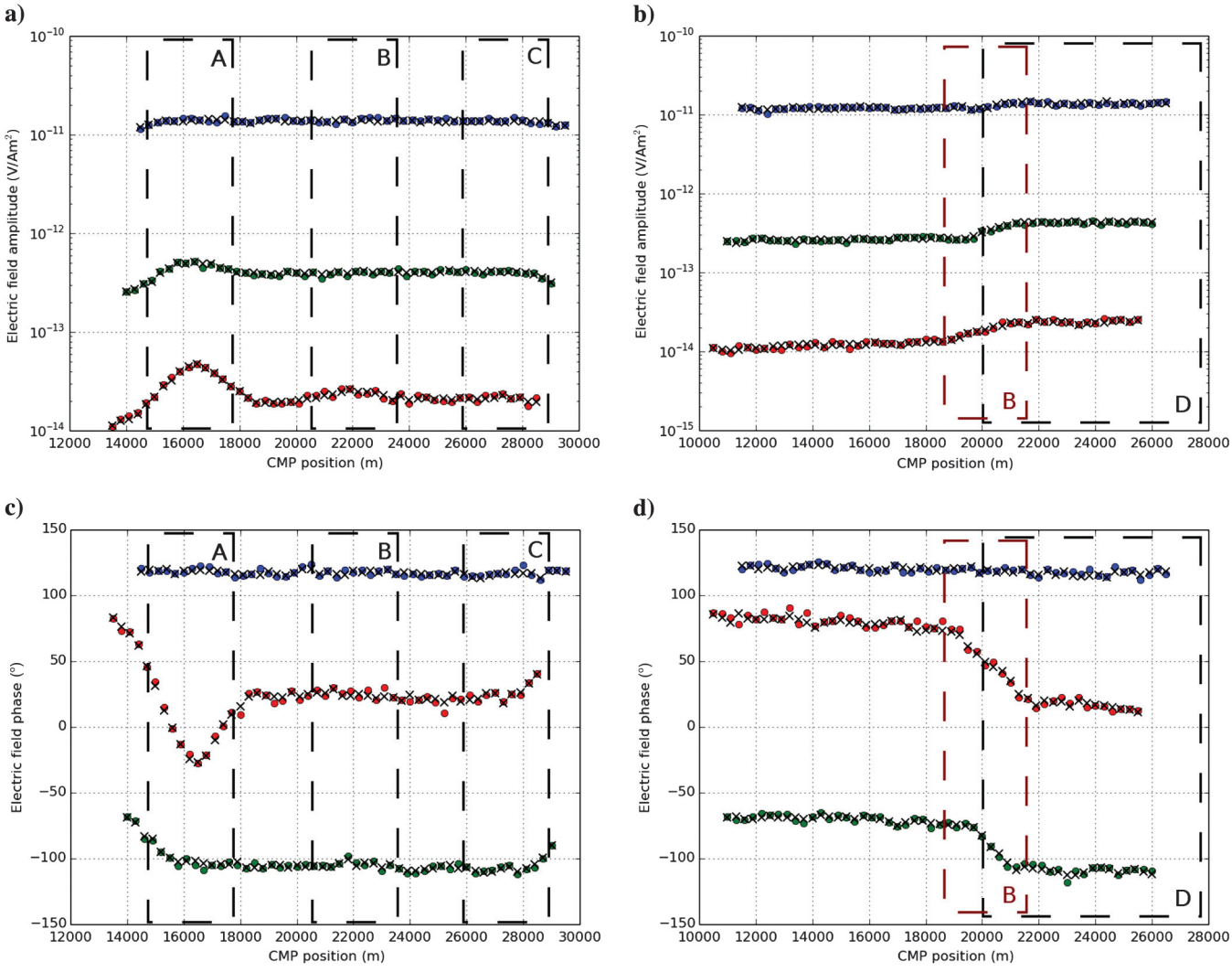

Figure 5. Towed receiver amplitude and phase data at 3.2 Hz for (a and c) cross section 1-1′ and (b and d) cross section 2–2′ (see Figure 2). The fixed-offset data are plotted at the CMP (the lateral midpoint between the center of the dipole antenna and the receiver) position along the towline with the following color coding: blue, 1-km offset; green, 2-km offset; and red, 3-km offsets. The dashed line annotation indicates the spatial location of the resistors A-C and D from Figure 2. The noise floor is at 10^{-15} V/Am^2; i.e., it is outside the scale of the amplitude plots. The filled circles are the inversion input data obtained by contaminating the synthetic data from the true model with noise according to 2. The black crosses represent the corresponding synthetic data from the inversion of the combined data set with stationary and towed receivers. For most data points, the crosses overlap the circles and can be difficult to see.

the reconstruction is centered beneath the towlines, and it is very weak at locations in between towlines. This is due to the 2D nature of the data recorded by these receivers and the lack of sensitivity to features off the towline. Our results indicate that interpretation based on towed receiver data alone should only be done on cross sections along one of the survey towlines (note that for seabed receivers, the azimuth data recorded from source towlines offset from the line of receivers introduces lateral coverage in between towlines). Figure 7c and 7d shows that the thickness resolution is also greatly improved compared to the result using only seabed receiver data. Resistor D is clearly resolved also in the region where there is lateral overlap with target A, which is buried just 550 m below the base of resistor D.

The reconstruction of resistor D using towed receiver data exhibits some spatial inhomogeneity. This is mainly caused by the noise added to the data, as explained above. The same type of artifact is not as pronounced for reconstructions using seabed receiver data. This is due to the higher noise levels in towed receiver data, but it is also because of the low data fold so that the stacking power in the inversion is low.

Figure 6c shows that the inversion using both data types was able to preserve the consistent imaging along towlines due to towed receiver data, and there is also a small effect of improving the reconstruction in regions not directly beneath towlines due to the 3D coverage from the seabed receiver data. We consider the improvement to the resistor D imaging to be sufficient that, given an exploration scenario, the geologic interpretation of the feature could be different. This illustrates the value of the imaging improvement from the towed receiver data in this case.

Let us now consider the imaging results for the deeper targets A-C. The inversion result obtained from the seabed receivers, Figure 7a, resolved all the deep targets with the approximate correct transverse resistance and depth. The transverse resistance is the depth integral of the thickness and resistivity, and it corresponds to 10^4 Ωm^2 for targets A-C. The geometry of target A is somewhat distorted due to the limited sampling of the sparse receiver grid. The thickness resolution for target C is not as good as that for target A. This is because the higher frequencies are less sensitive to the deepest target due to signal attenuation in the conductive overburden.

As we can see from Figure 7c, the towed receiver data lack sufficient information to properly reconstruct the deeply buried targets B and C. This is due to the limited offset range of the towed receiver array, but also the higher noise levels. Moreover, if we consider cross sections that are not aligned with any of the towlines, yet they cross over target A, the reconstruction of target A is absent. This effect is due to the 2D coverage discussed above in relation to the resistor D imaging results.

When we combine the data sets, we see that the resolution of the deep targets from the seabed receiver data is preserved, along with the improved shallow resistor imaging from towed receiver data.

The lateral overlap of resistor D with the targets A-C is expected to be a complication for the inversion. The Figure 7 cross sections (e and f) show a slightly deteriorated imaging result where the target overlaps with resistor D. However, the reconstructions of the targets are clearly separated from resistor D.

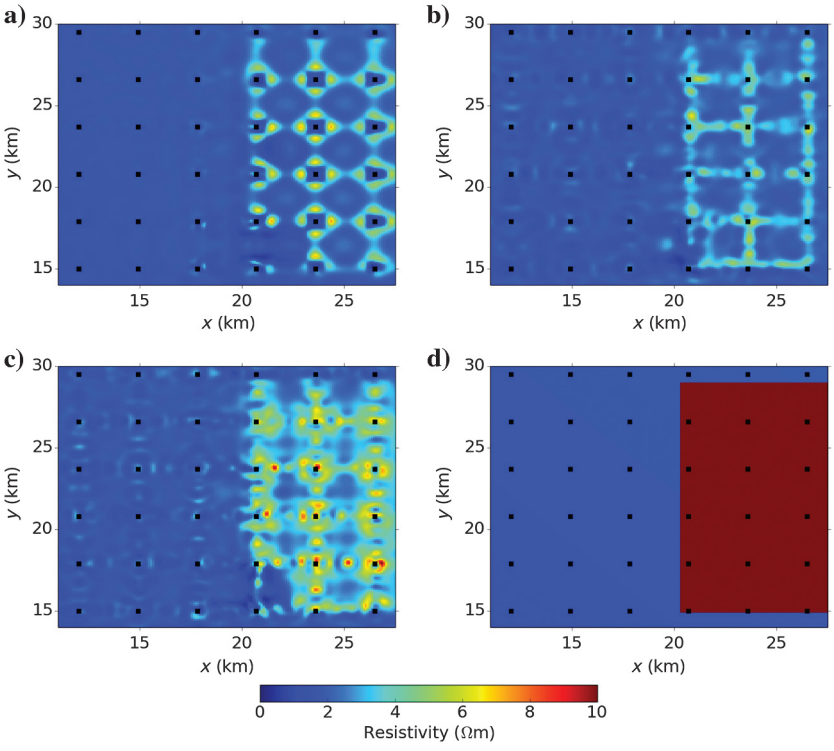

Figure 6. Depth slices at $z = 1400$ m for (a) inversion result using only data from seabed receivers, (b) inversion result using only data from towed receivers, (c) inversion result using data from the seabed and towed receivers, and (d) the true model. The bottom color scale applies to all plots, and it shows resistivity in Ωm . The black squares show the towline crossing points (coinciding with the seabed receiver positions) as a visual aid; see Figure 2.

Imaging criteria and offset sampling

The imaging results achieved by 3D inversion shown in Figures 6 and 7 demonstrate that to properly recover the shape of the shallow resistive feature, data must be sampled over a wide range of offsets including short offsets 1–3 km. The seabed and the towed receiver data sets have sensitivity toward the shallow resistor (see Figures 4 and 5), and the predicted responses from the inversion model agree with the data. However, the shape is poorly represented in the result from seabed receivers only, even along the source towlines.

In particular, the reconstruction of resistor D directly underneath the seabed receivers is far from the true model. Although this region is close to the receiver and one could expect high sensitivity, Figure 4 shows that the data are sensitive to the presence of resistor D only at offsets of greater than 1 km. This is because the measurement is dominated by direct propagation through seawater or along the seafloor for the shorter ranges. Thus, the CMP positions of data points sensitive to resistor D are at least 0.5 km away from the receiver location, which coincides with the onset of the reconstruction in Figure 6a. In a denser seabed receiver grid, sensitive data at CMP position over a given receiver position would be provided by

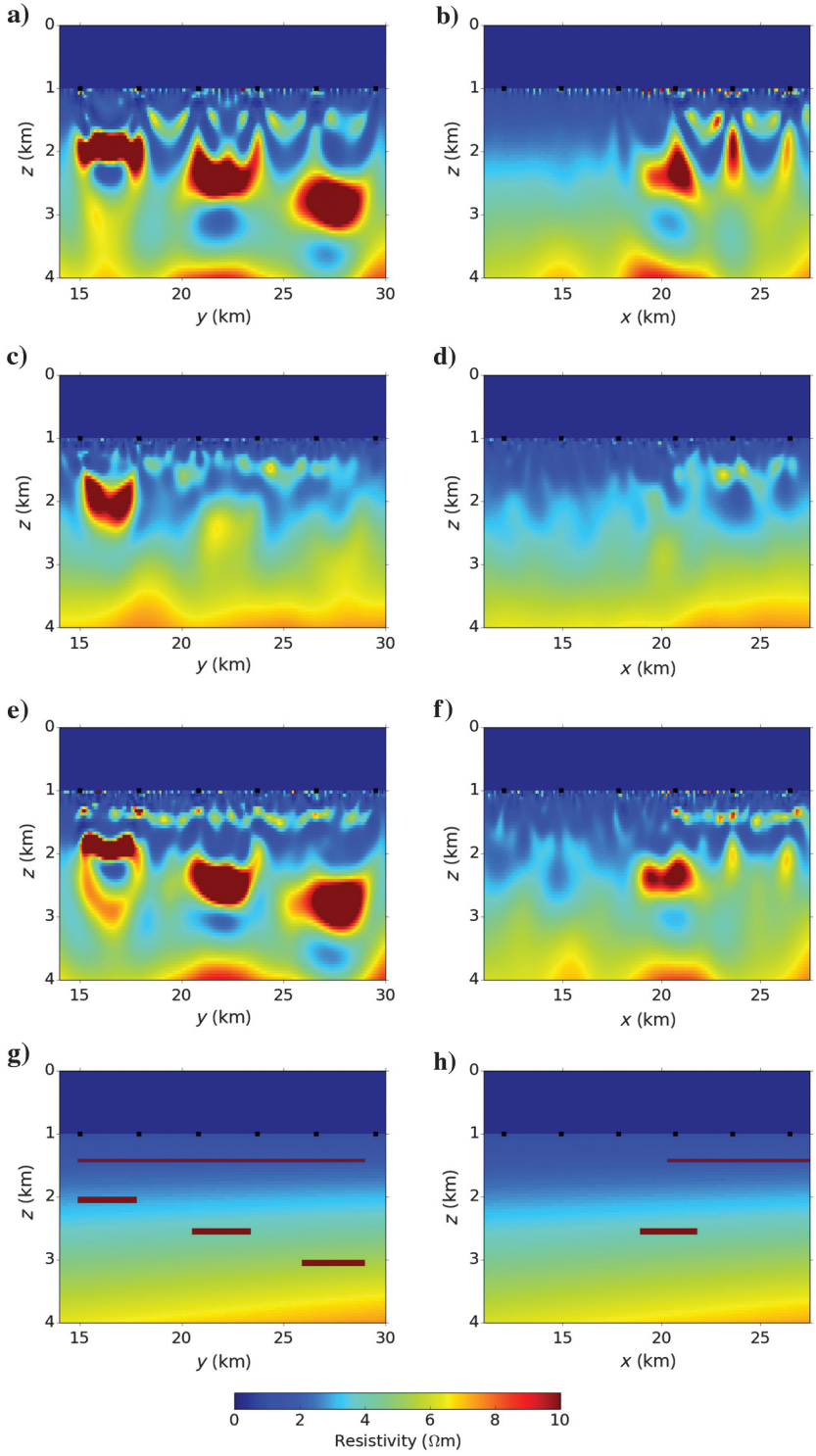

Figure 7. The left column shows cross sections along the *y*-direction, and the right column shows cross sections along the *x*-direction (marked 1-1′ and 2-2′ in Figure 2) for the (a and b) inversion result using only data from seabed receivers, (c and d) inversion result using only data from towed receivers, (e and f) inversion result using data from the seabed and towed receivers, and the (g and h) true model. The bottom color scale applies to all plots, and it shows resistivity in Ωm. The black squares show the towline crossing points (coinciding with seabed receiver positions) as a visual aid; see Figure 2.

neighboring receivers. In the joint seabed and towed receiver inversion considered in this paper, these data are provided by the towed receivers.

Although there are no data with CMP position underneath the seabed receivers in the seabed-receiver-only data set, the part of resistor D located there contributes to the response in the data. Inspection of the depth range 1.5–2 km in Figure 7b reveals that resistive features directly underneath the receivers were introduced by the inversion to fit the data. So the parts of resistor D located underneath the seabed receivers contribute to the response. However, insufficient information was available in the data to reconstruct the resistor at the true depth and with a geometry consistent with the reconstruction at other locations.

Note that the situation for resistor D imaging discussed above is different for the case of imaging targets B and C from the towed receiver data. For these targets, the towed receiver data do not have a measurable response to the given accuracy, and therefore no resistor needs to be introduced in the model to fit the data.

The observations above regarding offset range sampling is in correspondence with a more general imaging criterion. Data sensitivity is a necessary condition, but it is not a sufficient condition for successful imaging (Mittet and Morten, 2012). We further require that the data sensitive to the feature we want to image has the dynamic range appropriate to sample the geometry. In the example studied in this paper, this imaging issue is resolved by extending the range of offsets.

CONCLUSIONS

Cost-effective, coarse-grid 3D CSEM is typically deployed for frontier exploration. Although it gives good sensitivity and imaging results for deeply buried hydrocarbon targets, the limited amount of short-offset data samples from such grids may lead to unsatisfactory resolution of shallow resistors. We considered augmenting such surveys with data from an array of receivers towed at fixed offsets behind the source. The towed receiver array data are acquired at the same time as the stationary seabed receiver data are acquired, such that the additional vessel time used for the survey is short. In our synthetic study, we use a realistic noise model. The different noise levels in data from towed and seabed receivers reflect the operational character of the different equipment sets. Our 3D inversion results show that the data from the towed receiver array are useful for shallow resistor imaging and can significantly enhance the imaging result. However, the data coverage is only in 2D, which means that the geometry in between towlines is

not accurately recovered and the imaging improvement is only apparent in cross sections aligned with a towline. The towed receiver data alone are not sensitive to deeply buried hydrocarbon targets. However, when we combine the towed receiver data with data from seabed receivers, we achieve an enhanced imaging of shallow resistors along towlines, as well as maintaining the 3D resolution of the deeply buried hydrocarbon targets.

ACKNOWLEDGMENTS

We wish to thank EMGS for the permission to publish these results. JPM acknowledges support from the Research Council of Norway. JPM also thanks the Institute of Geophysics and Planetary Physics at Scripps Institution of Oceanography for graciously hosting him while the manuscript was being completed. We further thank the anonymous reviewers for numerous suggestions that helped us to improve our manuscript.

REFERENCES

Constable, S., P. Kannberg, K. Callaway, and D. R. Meija, 2012, Mapping shallow geological structure with towed marine CSEM receivers: 82nd Annual International Meeting, SEG, Expanded Abstracts, doi: 10.1190/segam2012-0839.1.

Constable, S., and L. J. Srnka, 2007, An introduction to marine controlled-source electromagnetic methods for hydrocarbon exploration: Geophysics, **72**, no. 2, WA3–WA12, doi: 10.1190/1.2432483.

Gabrielsen, P. T., P. Abrahamson, M. Panzner, S. Fanavoll, and S. Ellingsrud, 2013, Exploring frontier areas using 2D seismic and 3D CSEM data, as exemplified by multi-client data over the Skrugard and Havis discoveries in the Barents Sea: First Break, **31**, 63–71.

Goswami, B., K. Weitemeyer, T. Minshull, M. Sinha, and G. Westbrook, 2013, CSEM survey of a methane vent site, offshore West Svalbard: Fire in the Ice: Methane Hydrate Newsletter, **13**, no. 2, 12–18.

Løseth, L. O., 2011, Insight into the marine controlled-source electromagnetic signal propagation: Geophysical Prospecting, **59**, 145–160, doi: 10.1111/j.1365-2478.2010.00898.x.

Maaø, F., 2007, Fast finite-difference time-domain modeling of marine-subsurface electromagnetic problems: Geophysics, **72**, no. 2, A19–A23, doi: 10.1190/1.2434781.

Mattsson, J., G. Hall, E. Björnemo, A. McKay, M. Ronaess, and C. Anderson, 2012, Error analysis and capability modelling for towed streamer electromagnetics: First Break, **30**, 91–96.

Mittet, R., H. Maulana, K. Brauti, and T. Wicklund, 2007, CMP inversion of Marine CSEM data: Presented at the EGM International Workshop.

Mittet, R., and J. Morten, 2012, Detection and imaging sensitivity of the marine CSEM method: Geophysics, **77**, no. 6E411–E425, doi: 10.1190/geo2012-0016.1.

Morten, J. P., A. K. Bjørke, T. Støren, E. Coward, S. A. Karlsen, and F. Roth, 2009, Importance of azimuth data for 3D inversion of marine CSEM scanning data: 71st Annual International Conference and Exhibition, EAGE, Extended Abstracts, X005.

Weitemeyer, K., and S. Constable, 2010, Mapping shallow geology and gas hydrate with marine CSEM surveys: First Break, **28**, 97–102.

Weitemeyer, K., and S. Constable, 2012, Marine electromagnetic methods for gas hydrate characterization: Presented at the Offshore Technology Conference, 23698.

Xu, W., and C. Ruppel, 1999, Predicting the occurrence, distribution, and evolution of methane gas hydrate in porous marine sediments: Journal of Geophysical Research, **104**, 5081–5095, doi: 10.1029/1998JB900092.

Zhu, C., H. Byrd, and J. Nocedal, 1997, L-BFGS-B: Algorithm 778: L-BFGS-B, FORTRAN routines for large scale bound constrained optimization: ACM Transactions on Mathematical Software, **23**, 550–560, doi: 10.1145/279232.279236.